Flux-Pinned Dynamics Model Parameterization and Sensitivity Study

Frances Zhu[†]

Cornell University

452 Upson Hall

Ithaca, NY 14853

Mason Peck[‡]

Cornell University

455 Upson Hall

Ithaca, NY 14853

Laura Jones-Wilson[*]

Jet Propulsion Laboratory,

California Institute of Technology

4800 Oak Grove Dr.

Pasadena, CA 91109

Abstract— **Flux-pinned interfaces maintain a passively stable equilibrium between two spacecraft in close-proximity. Although flux-pinning physics has been studied from a materials-science perspective and at the systems level, the sensitivities and implications of system-level designs on the dynamics need to be better understood, especially in interfaces with multiple magnets and superconductors. These interfaces have highly nonlinear, coupled dynamics that are influenced by physical parameters including strength of magnetic field sources, field-cooled position, and superconductor geometry. Kordyuk's frozen image model successfully approximates the characteristics of flux pinning dynamics but could provide more precise state prediction with the addition of these physical parameter refinements. This paper addresses that gap by offering parametric terms to improve the dynamics model, which may better simulate the behavior of a multiple-magnet-multiple-superconductor interface. The sensitivity of the general flux-pinned dynamics model is studied by varying the physical parameters and simulating the systems level dynamics. This work represents a critical step in the development of a model suited to spacecraft performance verification.**

Index Terms—**Dynamics, electromagnetic effects, superconducting magnets, close-proximity spacecraft**

NOMENCLATURE

$a_\#, b_\#, c_\#, d_\#$ coefficients dictating vertical and horizontal image strength due to hysteresis

B_a magnetic field penetrating the superconductor at its boundary

---

[†] AIAA Student Member, Graduate Student, fz55@cornell.edu
[‡] AIAA Member, Associate Professor, mp336@cornell.edu
[*] Guidance and Control Systems Engineer, Laura.L.Jones@jpl.nasa.gov

B_c	minimum critical threshold magnetic field
B_0	magnetic field surface strength of the source magnet
c_d	rate of reduction from spatial relationship between magnet and superconductor
c_D	coefficient of reduction from spatial relationship between magnet and superconductor
c_g	coefficient of grain alignment, capturing the percentage of image strength at alignment θ
c_{max}	coefficient of reduction in which the magnet is directly centered and normal to the superconductor's surface
c_t	coefficient of temperature, capturing the percentage of image strength at temperature T with respect to T_{ref}
F	attractive force from flux-pinned interaction
h	vertical position of physical magnet from the surface of the superconductor
$k_l\ k_h\ k_\theta$	stiffness in lateral, normal, and rotational degrees of freedom
l	horizontal displacement of physical magnet from the center of the superconductor
$\boldsymbol{m}_f$	magnetic moment dipole of magnet's frozen image
$\boldsymbol{m}_{FC}$	magnetic moment dipole of physical magnet during field-cooling process
$\boldsymbol{m}_h$	magnetic moment dipole of magnet's horizontal image
$\boldsymbol{m}_m$	magnetic moment dipole of magnet's mobile image
$\boldsymbol{m}_{mag}$	magnetic moment dipole of physical magnet
$\boldsymbol{m}_v$	magnetic moment dipole of magnet's vertical image
m_0	maximum magnitude of magnetic moment dipole measured at $\theta = 0°$
m_{90}	minimum magnitude of magnetic moment dipole measured at $\theta = 90°$
$\boldsymbol{O}_s$	specified origin
$\boldsymbol{\rho}_f$	displacement vector from magnet's frozen image to physical magnet
$\boldsymbol{\rho}_m$	displacement vector from magnet's mobile image to physical magnet
$q_x\ q_y\ q_z\ q_s$	spacecraft attitude
$\boldsymbol{r}_f$	position vector of magnet's frozen image from specified origin
$\boldsymbol{r}_{FC}$	position vector of physical magnet during field-cooling process from specified origin
$\boldsymbol{r}_m$	position vector of magnet's mobile image from specified origin
$\boldsymbol{r}_{mag}$	position vector of physical magnet from specified origin

T operational temperature of the superconductor

T_{ref} reference temperature of the superconductor

θ relative alignment between the superconductor surface and magnetic moment dipole pole axis

θ_{FC} angular displacement from the ideal field-cooled attitude

U magnetic potential energy

$v_x\ v_y\ v_z$ spacecraft velocity

$\omega_x\ \omega_y\ \omega_z$ spacecraft angular velocity

$\omega_l\ \omega_h\ \omega_\theta$ natural angular velocity in lateral, normal, and rotational degrees of freedom

$x\ y\ z$ spacecraft position

$x_{FC}\ z_{FC}$ spacecraft position displacement from the ideal field-cooled position

TABLE OF CONTENTS

1. INTRODUCTION

Flux-pinned interfaces leverage the dynamics of magnetic flux pinning to control the relative orientation and position of close-proximity spacecraft without mechanical contact. These unique traits make flux-pinned interfaces a technology candidate for applications such as spacecraft capture and docking[1,2], assembly of modular systems[3,4], formation flying[5–7], kinematic mechanisms[8,9], and station-keeping[10,11]. However, for this technology to be mature enough for spaceflight applications, its physics must be represented in a high-fidelity predictive dynamics model that

can inform design trade and analyses. Current closed-form dynamics models of the interactions express the basics of the interaction qualitatively but are too coarse to meet the needs of the design process. This gap motivates the development of tools to empirically modify existing dynamics models so that the refinements better predict time and frequency responses for space systems featuring a flux-pinned interface.

2. BACKGROUND

Flux Pinning Magnetization Models

In a system of magnets and type-II superconductors, conventional methods of modeling magnetization behavior include Bean's critical state model and Kordyuk's advanced frozen image model. Both macroscopically represent changes in the superconductor's embedded magnetic field as the external field changes but express the magnetization differently. The critical-state model expresses the internal magnetic field as a distribution of electron current vortices at the superconductor boundary[12]. The frozen image model geometrically maps a magnetic moment dipole into paramagnetic and diamagnetic images reflected across the superconductor boundary that move virtually within the superconductor volume[13].

The two methods differ in complexity and scope. The critical-state model superimposes a multitude of magnetization loops to represent a magnetic source. This model increases in accuracy and fidelity as the resolution of magnetization loops is refined but is also more numerically intensive[14]. Due to its numerical nature, the critical-state model is valid for an arbitrary superconductor geometry and magnetic field gradient. The computational complexity of the critical-state model may be restrictive for real-time applications and systems of many magnets and superconductors.

The frozen image model generates two virtual magnetic moment dipoles for each independent magnet and superconductor interaction. Two closed-form analytical image representations drastically simplify the macroscopic behavior, especially for a system of multiple magnets and superconductors. The frozen image model is simple enough to simulate real time dynamics, which have natural modes as fast as hundreds of Hertz.

For a system of M superconductors and N magnets, the frozen image model offers the simplicity of a closed-form solution to the dynamics with computation processes at an order of $\sigma(MN^2)$. In contrast, the critical state model not only compounds across every superconductor and magnet, but also across every mesh node P of each object, at an order of $\sigma(MP_M^2N^2P_N^4)$, which requires an immense amount of computation. The frozen image model is limited in its

assumptions about the superconducting system that reduce the model's fidelity and breadth of applicability. This paper incorporates deeper knowledge of parametric effects to increase model fidelity while minimizing the computational processes within the same magnitude as $\sigma(MN^2)$.

Frozen Image Model Derivation

We follow Kordyuk's derivation of the frozen image model and test the assumptions laid out in his derivation. Once a type-II superconductor is cooled below its critical temperature, Kordyuk's model creates two images: the frozen image and the mobile image. For a magnet field-cooled with initial position r_{FC} and magnetic moment m_{FC}, the frozen image position is r_f and magnetic moment m_f, as shown in Figure 1. The frozen image remains static while the mobile image moves with its magnetic field source, reflecting both the physical magnet's position (r_{mag}) and orientation (m_{mag}) across the superconductor surface. ρ_m is the distance between the corresponding mobile image and magnet, ρ_f the frozen image to magnet. The following equations form the basis of the frozen image model, maintaining the external magnetic field gradient in the presence of disturbances.
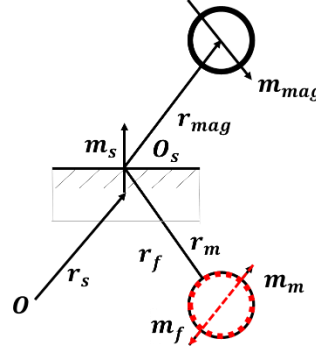
Figure 1: Geometric relationship of frozen image, mobile image, superconductor and magnet in equilibrium; a unique configuration in which $r_{mag} = r_{FC}$ and $m_{mag} = m_{FC}$ [2].

$$H_z(\rho - r_{FC}, m_{FC}) = H_z(\rho - r_f, -m_f) \tag{1}$$

$$H_z(\rho - r_{mag}, m_{mag}) + H_z(\rho - r_m, -m_m) = 0 \tag{2}$$

The external magnetic field H_z of the permanent magnet is equivalent to the internal magnetic field of the frozen image within the superconductor upon the process of field-cooling a frozen image into the superconductor, as shown in Eq. (1). The magnetic field contribution H_z from both the magnet and mobile image sum to no net magnetic field

disturbance, represented by Eq. (2). These equations form the basis for dynamics derivations and carry a series of fundamental assumptions that are discussed below.

The frozen image magnetic moment dipole is defined by the field-cooled magnet's position and strength, in which important geometric parameters are not included. Eq. (1) assumes the frozen image dipole is of the same strength as the magnet dipole field-cooled to the superconductor, a one-to-one mapping. A comparable representation of the magnetization behavior is the percentage of total magnetic flux from the source dipole penetrating the volume of the superconductor. The relative size of the magnet and superconductor scales the percentage of flux captured in the superconductor[15]. The embedded magnetic field is agnostic to the location of the field-cooled magnet, which is valid for an infinite plane, but invalid for a superconductor of finite surface[16]. The magnet's location relative to the superconductor surface also determines the strength of the frozen image. Eq. (1) does not address any of these effects on the frozen image.

In an ideal superconductor, the mobile image exactly compensates for a change in magnetic field, the source magnet. The ideal superconductor expels all disturbances, but for a real superconductor, the magnetic field may penetrate through the superconductor boundary, implying that the right side of Eq. (2) is nonzero. Much like the frozen image, the mobile image is defined by the source magnet's position and orientation and is affected by the same geometric parameters: relative geometry, the magnet source's relative position, and orientation. The source magnet may also generate a mobile image of differing strength upon approach and exit but does not permanently change the system, a manifestation of elastic magnetic hysteresis[17,18,19]. The source magnet may permanently change the embedded magnetic field after field-cooling in a process called flux creep or plastic magnetic hysteresis[20,21,22]. Analogously, Eq. (2) does not address these effects on the mobile image.

Outside the fundamental physics, the explicit geometric expressions also carry underlying assumptions. Equations (5) to (10) formalize both images' magnetic moment dipoles as a geometric function of position and orientation of both the source magnet and superconductor, depicted geometrically in Figure 1. Subscript m and f correspond to the mobile image and frozen image, respectively. $\hat{m}_s$ is the unit direction normal to the surface of the superconductor. ρ_f and ρ_m is the distance from the image to the source magnet, where r_f and r_m is the location of the image and O_s is an arbitrary point on the superconductor surface. This formulation assumes that the strength, orientation, and location of the frozen image map one to one with the field-cooled magnet and remain fixed. Many of

the same assumptions from Eq. (1) apply to Eq. (3) and Eq. (6).

In these equations, the superconductor orientation and location relate explicitly to the image definition. By using $\widehat{\boldsymbol{m}}_s$ to represent the direction normal to the superconductor surface in Eq. (3) and (4), Kordyuk assumes that the superconductor plane is flat, without manufacturer defects, and of single domain[23,24]. On an infinite superconductor plane, $\boldsymbol{O}_s$ serves as a reference point that is arbitrarily placed. This reference point must be strategically placed on a finite surface of the superconductor due to the reference point's effect on representing total flux captured in the superconductor volume. The full geometric definition of the images is then used in the governing equations of motion.

$$m_f \; = \; \left(2\widehat{\boldsymbol{m}}_s \otimes \widehat{\boldsymbol{m}}_s - \underline{\boldsymbol{1}}\right)m_{mag} \tag{3}$$

$$\boldsymbol{\rho}_f = \; \boldsymbol{r}_{FC} - \boldsymbol{r}_f \tag{4}$$

$$\boldsymbol{r}_f = \boldsymbol{r}_{FC} - 2\left((\boldsymbol{r}_{FC} - \boldsymbol{O}_s)\cdot\widehat{\boldsymbol{m}}_s\right)\widehat{\boldsymbol{m}}_s \tag{5}$$

$$m_m \; = \; \left(\underline{\boldsymbol{1}} - 2\widehat{\boldsymbol{m}}_s \otimes \widehat{\boldsymbol{m}}_s\right)m_{mag} \tag{6}$$

$$\boldsymbol{\rho}_m = \; \boldsymbol{r}_{mag} - \boldsymbol{r}_m \tag{7}$$

$$\boldsymbol{r}_m = \boldsymbol{r}_{mag} - 2\left((\boldsymbol{r}_{mag} - \boldsymbol{O}_s)\cdot\widehat{\boldsymbol{m}}_s\right)\widehat{\boldsymbol{m}}_s \tag{8}$$

Governing Equations of Motion

To create a dynamics model incorporating flux-pinned interactions, the frozen image model is combined with Villani/Landecker's analytic solutions for force and torque between two magnet dipoles[25,26]. The force and torque of a magnetic dipole $\boldsymbol{m}_b$ acting on another magnetic dipole $\boldsymbol{m}_a$ at distance $\boldsymbol{\rho}$ is reiterated in Eq. (9) and (10). The sum of force and torque on a rigid body is reiterated in Eq. (11) and (13) to illustrate that the sum of influence from a flux pinning interaction only includes two components: frozen and mobile image. The parametric effects affect the expression and summation of force and torque but do not ultimately affect the governing equations of motion so the remaining derivation is not repeated here, but may be referenced[27]. For a rigid body with *M* static superconductors interacting with a rigid body of *N* magnets, the total force and torque acting on the body is the sum of every source magnet interaction across every image, across all superconductors. Any modifications on the general interaction between a source magnet and image is compounded across *M* superconductors, 2*N* magnet images, and *N* source magnets, a resultant magnification of $2MN^2$.

$$\boldsymbol{F}_{ab} = \frac{3\mu_0 m_a m_b}{4\pi\rho^4}\left((\widehat{\boldsymbol{\rho}}\times\widehat{\boldsymbol{m}}_a)\times\widehat{\boldsymbol{m}}_b + (\widehat{\boldsymbol{\rho}}\times\widehat{\boldsymbol{m}}_b)\times\widehat{\boldsymbol{m}}_a - 2\widehat{\boldsymbol{\rho}}(\widehat{\boldsymbol{m}}_a\cdot\widehat{\boldsymbol{m}}_b) + 5\widehat{\boldsymbol{\rho}}\left((\widehat{\boldsymbol{\rho}}\times\widehat{\boldsymbol{m}}_a)\cdot(\widehat{\boldsymbol{\rho}}\times\widehat{\boldsymbol{m}}_b)\right)\right) \tag{9}$$

$$\boldsymbol{\tau}_{ab} = \frac{\mu_0 m_a m_b}{4\pi \rho^3} \left(3(\hat{\boldsymbol{m}}_a \cdot \hat{\boldsymbol{\rho}})(\hat{\boldsymbol{m}}_b \times \hat{\boldsymbol{\rho}}) + (\hat{\boldsymbol{m}}_a \times \hat{\boldsymbol{m}}_b) \right) \tag{10}$$

$$\boldsymbol{F}_i = \sum_{j=1}^{N} \sum_{k=1}^{M} \left(\left(\boldsymbol{F}_{frozen} + \boldsymbol{F}_{mobile} \right)_k \right)_j \tag{11}$$

$$\boldsymbol{F}_{COM} = \sum_{i=1}^{N} \sum_{j=1}^{N} \sum_{k=1}^{M} \left(\left(\left(\boldsymbol{F}_{frozen} + \boldsymbol{F}_{mobile} \right)_k \right)_j \right)_i \tag{12}$$

$$\boldsymbol{\tau}_{COM} = \sum_{i=1}^{N} \sum_{j=1}^{N} \sum_{k=1}^{M} \left(\left(\left(\boldsymbol{\tau}_{frozen} + \boldsymbol{\tau}_{mobile} \right)_k \right)_j \right)_i + \sum_{i=1}^{M} \boldsymbol{\rho}_i \times \boldsymbol{F}_i \tag{13}$$

3. Parameter Identification in Application

This section reviews the assumptions from the frozen image model in depth, surveys the supporting literature that extends the basic model, and offers a mathematical formulation to account for these effects in the dynamics model. The physical properties that affect the frozen image model are temperature, material properties, manufacturing process, hysteresis, geometric and spatial relationships.

Temperature

Temperature affects flux pinning interactions in three ways: maximum levitation stiffness, physics activation, and elastic hysteresis. Unlike Kordyuk's assumption of binary activation in superconductors, observations suggest the superconducting phenomenon is continuously activated. Chiang and Jiang both found that the colder the superconductor, the more levitation stiffness and less hysteresis are emphasized in the force curves[28,29]. Although both investigators studied YBCO samples, the relationship between levitation force and temperature disagree, as seen in Figure 2. The discrepancy may lie in the samples. Chiang used superconductor samples on the scale of two to three millimeters with a magnet much larger than the superconductor (roughly four times the surface area), whereas Jiang used a superconductor 30 mm in diameter and a magnet slightly smaller than the superconductor. For the small superconductor samples, the hysteresis gaps are very evident and temperature variation does not taper off, but seemingly extends linearly. For the large superconductor samples, the temperature variation tends to taper off as the superconductor reaches 40 K and hysteresis affects the force path negligibly. A general trend may be drawn, that colder temperatures offer stronger interactions, but a precise scaling factor cannot be extrapolated from these two studies.
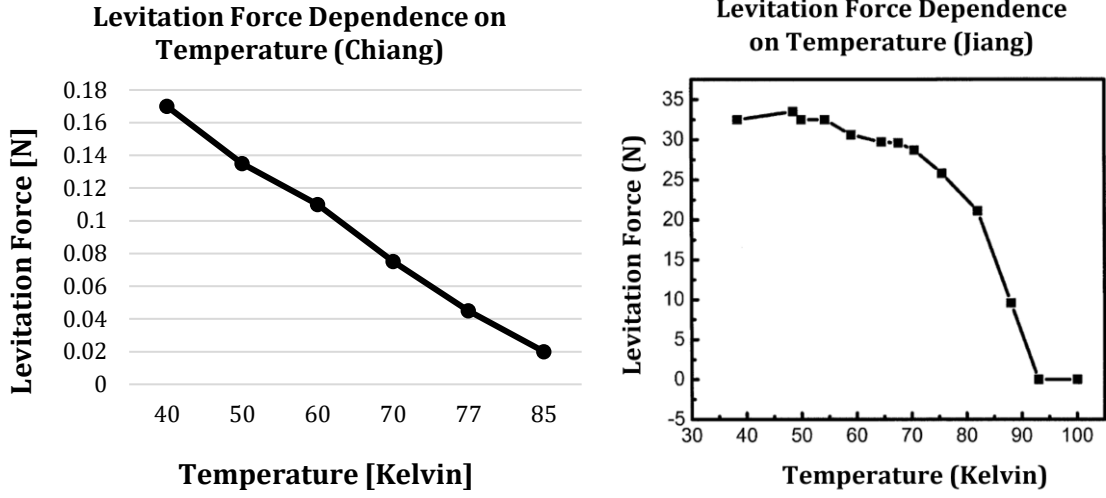
Figure 2: Comparison of Chiang and Jiang's results on levitation force and temperature relationship [1] [2].

To incorporate temperature variation into the dynamics model, the formulation for the mobile and frozen image magnetic moment dipoles include a scaling factor $c_t(T|T_{ref})$ given by Eq. (14) and (15). T is the temperature in which the superconductor operates and T_{ref} is the reference temperature in which the levitation force was measured, separated by the condition given operator '|'. c_t is greater than 1 when $T < T_{ref}$, less than 1 when $T > T_{ref}$, and equal to 1 when $T = T_{ref}$. $c_t(T|T_{ref})$ can be found through interpolation or extrapolation of the empirical dataset provided by Chiang or Jiang[28,29], but due to the disagreement, the most accurate method to determine the scaling factor is to measure the temperature variation for each specific magnet and superconductor used in a given application. Intuitively, the variation in temperature scales the strength of the interaction.

$$m_m = c_t(T|T_{ref})\left(\underline{1} - 2\widehat{m}_s \otimes \widehat{m}_s\right)(m_{mag}) \tag{14}$$

$$m_f = c_t(T|T_{ref})\left(2\widehat{m}_s \otimes \widehat{m}_s - \underline{1}\right)(m_{FC}) \tag{15}$$

Material Properties

The material properties of the superconductor vary the behavior of the flux-pinned interaction immensely, ranging from the elemental composition, manufacturing process, and crystalline structure. The elemental composition affects the critical temperature at which the superconductor is superconducting, its lower and upper critical field, and the critical current density[30]. Yttrium Barium Copper Oxide (YBCO) has been studied extensively due to its heritage, high critical temperature, and high critical magnetic fields. In addition, YBCO superconductor discs exhibit flux pinning

above liquid nitrogen's boiling temperature, requiring only inexpensive and widely accessible technology. YBCO also has no known material safety hazards[31]. When modeling the dynamics, the lower critical magnetic field bounds affect the interaction continuity. The higher critical magnetic field bounds affect the strength of the interaction. And finally, hysteresis affects the predictability of the system.

An intrinsic property of a superconductor is its elemental composition. Important energy parameters like critical temperature and thermodynamic critical field are defined by the material composition. At a microscopic level, the material affects the surface impedance at low fields, acting through intermediate-state tunneling, in which a lower threshold of critical field must be surpassed to give rise to any electromagnetic interaction. The weak tunnel coupling emphasizes anisotropy in different crystalline structures, such as copper, bismuth, or thallium planes[30]. For a YBCO sample structure (copper oxide planes) of specific temperature and geometry, the lower critical field is 0.1 T perpendicular to the plane and 0.02 T parallel to the plane[32]. The macroscopic geometry of the superconductor, such as surface area and volume shape, also play an important role in critical field thresholds and caution must be used when implementing these thresholds.

The lower critical field threshold effect is modeled as a discontinuous magnetic regime transitioning from no current excitation to current excitation. Treating the magnet as a singular dipole, the interaction is considered binary. Treating the magnet as a flux field, the interaction is better encapsulated as a continuous scaling of the dipole. B_a, the applied field, is the magnetic field penetrating the superconductor at its boundary. B_a is a function of the strength and orientation of the magnet dipole, the position with respect to the superconductor surface, and the superconductor surface normal. If B_a is above the minimum critical threshold B_c, there exists a virtual magnetic image that interacts with the source magnet, given by Eq. (16) and (17). The ultimate effect of material properties manifest as a critical field conditional that results in a binary interaction.

$$if\ B_a(\boldsymbol{m_{FC}}, \boldsymbol{r_{FC}}, \hat{\boldsymbol{m}}_s) > B_c, \quad then\ \boldsymbol{m_f} = (2\hat{\boldsymbol{m}}_s \otimes \hat{\boldsymbol{m}}_s - \underline{1})\boldsymbol{m_{FC}} \tag{16}$$

$$if\ B_a(\boldsymbol{m_{mag}}, \boldsymbol{r_{mag}}, \hat{\boldsymbol{m}}_s) > B_c, \quad then\ \boldsymbol{m_m} = (\underline{1} - 2\hat{\boldsymbol{m}}_s \otimes \hat{\boldsymbol{m}}_s)\boldsymbol{m_{mag}} \tag{17}$$

Manufacturing Process

A bulk superconductor may be made in different ways, ranging from compressing grains into a mold or inducing melt–textured growth of a single crystal in an oven. Manufacturing processes define intrinsic properties of the

superconductor. The internal structure and external geometry of the superconductor affect the strength and hysteretic behavior of the flux pinning physics.

Regardless of the manufacturing method, every superconductor has defects in its composition: surface smoothness, cracks, and impurities between copper planes[30]. Chan[33] fabricated superconducting samples with YBCO various sizes of grains and epoxy without aligning the grains to investigate the effects on critical current density, levitation force, and hysteresis. The larger grained samples had a lower current density, larger maximum levitation stiffness, and larger gap in the hysteresis curve. Similarly, Yang[23] sliced a large YBCO sample into smaller components to investigate the effect of different grain sizes on levitation stiffness, while retaining the same grain orientation. The smaller components, when reassembled to resemble the original disc, did not provide the same amount of levitation stiffness. The stiffness linearly decreased as a function of number of cuts/parts. Yang[24] explores the specific consequences of cracks in the superconductor sample, showing that the larger the crack, the less levitation stiffness the superconductor provided. Single-domain superconductors offer maximum levitation stiffness.

Grain alignment of a single-domain superconductor affects the strength of interaction and presence of hysteresis. After the raw sample is grown, the sample may be cut in different geometries with intended surface area aligned along the grain. The largest measured levitation stiffness occurs when the magnetic vector field is perpendicular to the copper planes, with a monotonic reduction of levitation force as the magnetic field becomes parallel with the copper planes[34–36]. The hysteresis gap is also observed to be largest when the copper planes are perpendicular to the applied field. The levitation force may be scaled as a function of relative alignment between the superconductor surface and magnetic moment dipole pole axis. Equation (18) characterizes this degradation, assuming the copper planes are parallel to the cut superconductor surface and the angle is zero when the moment dipole is aligned with the superconductor surface normal[35]. $\boldsymbol{m}$ is either image's magnetic moment dipole, a value scaled down by a function of angle between the dipole and superconductor normal in Eq. (19). The maximum magnitude of magnetic moment dipole m_0 is measured at $\theta = 0°$, and the minimum levitation force m_{90} is measured at $\theta = 90°$. The strength of the flux-pinned interaction is scaled by the relative orientation between the magnetic moment dipole and superconductor surface normal.

$$\boldsymbol{m} = c_g(\theta)m_0\hat{\boldsymbol{m}} \tag{18}$$

$$c_g(\theta) = \cos^2\theta + \frac{m_{90}}{m_0}\sin^2\theta \tag{19}$$

Hysteresis

The simplest dynamics model includes no hysteresis or negligible hysteresis, seen only in very cold flux-pinned interfaces[29]. At a higher temperature, the superconductor exhibits levitation whose force paths vary in elastic hysteresis and inelastic or plastic hysteresis. Hysteresis stems from elastic instabilities in the flux-line lattice that dissipates energy[20]. At a microscopic level, the flux line changes to a different energy state and dissipates through tiny eddy currents in the current vortices. Hysteresis that occurs during relative magnet-superconductor movement can bring the system to a continuous range of stable equilibria positions and orientations[17]. Some hysteresis is not recoverable, and plastic deformation in the internal magnetic field permanently changes the dynamic behavior of the system[20–22]. For the recoverable or elastic hysteresis curves, Zhang[18] and Yang[19] have proposed modifications to the frozen image model by including a vertical and horizontal movement image that even accounts for saturation within the superconducting material. The addition of the two scalable images accounts for the hysteresis gap.

Yang's full derivation is not repeated but the relevant additional image expressions are shown in Eq. (20) – (23) for insight. Eq. (20) is the vertical image expression as the magnet descends towards the superconductors, where h is the initial cooling position, h is vertical position, and h_0 is the lowest position. Eq. (21) is the counterpart vertical image expression for magnet ascension, where h_m is the highest position. Eq. (22) is the horizontal image expression as the magnet traverses farther from the center of the superconductor, where l is horizontal position. Eq. (23) is the counterpart horizontal image expression for a magnet moving closer to the field-cooled position, where l_m is the maximum horizontal displacement. All $a, b, c,$ and d terms are found by empirical data collected from the specific system of interest. The additional images influence the physical magnet in the same way as the frozen and mobile image, expressed with Villani's model. The additional image contributions are superimposed in the force and torque summations.

$$if \ \dot{h} < 0, \quad then \ \boldsymbol{m}_v = \left(- a_1(h - h_0) + a_2(h - h_0) \right) \widehat{\boldsymbol{m}}_v \tag{20}$$

$$if \ \dot{h} \geq 0, \quad then \ \boldsymbol{m}_v = \left(b_1(h_m - h_0) - b_2(h_m - h) \right) \widehat{\boldsymbol{m}}_v \tag{21}$$

$$if \ sign(\dot{l}) = sign(l), \quad then \ \boldsymbol{m}_h = c_1 l \ \widehat{\boldsymbol{m}}_h \tag{22}$$

$$if \ sign(\dot{l}) \neq sign(l), \quad then \ \boldsymbol{m}_h = \left(d_1 l_m - d_2(l_m - l) \right) \widehat{\boldsymbol{m}}_h \tag{23}$$

Geometric and Spatial Relationship

Extrinsic factors, such as geometry and spatial relationships, affect the way the source magnet flux penetrates the superconductor geometry, which then modifies the stiffness of the interaction. For example, the geometric mapping from a spherical source magnet to either image differs from that of a flat magnet[37]. Superconducting samples with the largest surface area and thickness offer the most levitation force. Thickness does not increase levitation force linearly but diminishes in rate of influence[38]. The optimal magnet size is slightly smaller than that of the superconductor; larger magnet diameters reduce the stiffness of the flux-pinned interaction[15]. The magnetic field shape of the source magnet affects the levitation force profiles, leading to stiffer interactions in which the gradient of the magnetic field changed drastically, like corners or sharp edges[39]. These higher-order effects are not accounted for in a dipole representation, and the magnetic moment dipole equation must be modified for the magnet of interest.

The spatial relationship between the magnet and superconductor influences the flux penetration within the superconductor, related to the minimum critical field. Kordyuk assumes an infinite plane superconductor but infinite geometries are nonphysical. A finite-dimension relationship requires a problem-specific formulation. As the equilibrium position of the source magnet moves farther from the center of the superconductor, the amount of flux penetrating the volume of the superconductor decreases, and thus the stiffness of the interaction also decreases[16]. Even when the magnet is field-cooled directly above the center of the superconductor, the frozen image strength is only 64% of the frozen image model anticipated strength. The strength of the images scales with distance from the center of the superconductor, given by Eq. (24) and (25). l, defined in Eq. (26), expresses the absolute distance from the center of the superconductor parallel to the surface of the superconductor and c_D, defined by Eq. (27), is a linear approximation of the degradation of strength as the magnet moves off the surface of the superconductor. c_D is found empirically where c_{max} is the portion of field captured in which the magnet is center above the superconductor and c_d is the reduction of field as a function of lateral distance l. Since the distance from the center of the superconductor is an important parameter in the flux-pinned system, Kordyuk's formulation of the distance vectors in Eq. (7) and (10) are modified to no longer use an arbitrary point as the reference origin O_s but to reference the center of the superconductor. The resulting coefficient, c_D, reduces the strength of flux-pinned interaction as the physical magnet moves laterally farther from the superconductor.

$$m_m = \left(\underline{1} - 2\widehat{m}_s \otimes \widehat{m}_s\right)\left(c_D(r_{mag})m_{mag}\right) \tag{24}$$

$$m_f = \left(2\hat{\boldsymbol{m}}_s \otimes \hat{\boldsymbol{m}}_s - \underline{1}\right)\left(c_D(\boldsymbol{r}_{FC})\boldsymbol{m}_{FC}\right) \tag{25}$$

$$l = |\boldsymbol{r} - (\boldsymbol{r} \cdot \hat{\boldsymbol{m}}_s)\hat{\boldsymbol{m}}_s| \tag{26}$$

$$c_D \approx c_{max} - c_d l \tag{27}$$

Summary

The physical properties of the magnet-superconductor system have significant consequences on the image expressions from Eq. (14) to (27). Reduction in magnetic field strength through temperature or geometric/spatial effects is embodied in scalar form, seen in Eq. (14) – (15), (18), and (249) – (25). The activation of flux pinning physics in different material properties is represented by a conditional statement, seen in Eq. (16) – (17). The higher order effects of hysteresis are captured in additional magnetic moment images, seen in Eq. (20) – (23). The physical parameters solely modify the magnetic moment dipole expressions for the frozen and mobile images. The superimposed effect of each parameter modification on the original magnetic moment dipole expressions are given in the Eq. (28) and (29). The dynamic behavior of the interface follows the summation of all individual image expressions (and their modifications). The revised expression for force and torque are given in Eq. (30) to (32), where the additional effects of the vertical and horizontal images are explicitly incorporated. The present study investigates the sensitivity of stiffness, energy, force, and natural frequency to small discrepancies in knowledge or control of these parameters.

$$\text{if } B_a(\boldsymbol{m}_{FC}, \boldsymbol{r}_{FC}, \hat{\boldsymbol{m}}_s) > B_c, \quad \text{then } \boldsymbol{m}_f = c_t(T|T_{ref})c_g(\theta)c_D(\boldsymbol{r}_{mag})\left(2\hat{\boldsymbol{m}}_s \otimes \hat{\boldsymbol{m}}_s - \underline{1}\right)\boldsymbol{m}_{FC} \tag{28}$$

$$\text{if } B_a(\boldsymbol{m}_{mag}, \boldsymbol{r}_{mag}, \hat{\boldsymbol{m}}_s) > B_c, \quad \text{then } \boldsymbol{m}_m = c_t(T|T_{ref})c_g(\theta)c_D(\boldsymbol{r}_{mag})\left(\underline{1} - 2\hat{\boldsymbol{m}}_s \otimes \hat{\boldsymbol{m}}_s\right)\boldsymbol{m}_{mag} \tag{29}$$

$$\boldsymbol{F}_i = \sum_{j=1}^{N}\sum_{k=1}^{M}\left(\left(\boldsymbol{F}_{frozen} + \boldsymbol{F}_{mobile} + \boldsymbol{F}_{vertical} + \boldsymbol{F}_{horizontal}\right)_k\right)_j \tag{30}$$

$$\boldsymbol{F}_{COM} = \sum_{i=1}^{N}\sum_{j=1}^{N}\sum_{k=1}^{M}\left(\left(\left(\boldsymbol{F}_{frozen} + \boldsymbol{F}_{mobile} + \boldsymbol{F}_{vertical} + \boldsymbol{F}_{horizontal}\right)_k\right)_j\right)_i \tag{31}$$

$$\boldsymbol{\tau}_{COM} = \sum_{i=1}^{N}\sum_{j=1}^{N}\sum_{k=1}^{M}\left(\left(\left(\boldsymbol{\tau}_{frozen} + \boldsymbol{\tau}_{mobile} + \boldsymbol{\tau}_{vertical} + \boldsymbol{\tau}_{horizontal}\right)_k\right)_j\right)_i + \sum_{i=1}^{M}\boldsymbol{\rho}_i \times \boldsymbol{F}_i \tag{32}$$

4. PARAMETERIZATION IN DESIGN AND MODEL FIDELITY

Physical Parameters Optimizing Performance

Design considerations at the systems level maximize stiffness in a practical flux-pinned interface. At a component level, the material properties of a superconductor dominate the operations and capabilities of flux-pinned interactions. The other side of the interface, the magnet, contributes to performance through its strength, size, and geometry. Other higher-level considerations include the relative size and location of the magnet and superconductor. The interface is

passive and contactless of which the magnetic spacecraft does not require any power and the superconducting spacecraft requires a thermal system to maintain the superconductors below 88K. Magnetic sensitive components or large magnetic field sources not involved in the flux-pinned interface should be shielded or located with enough distance. These physical parameters are selectable during system design and may optimize stiffness, but they do not impact the accuracy and fidelity of the dynamics model.

The most influential characteristic of a superconductor is its material, specifically its critical current density. Many different materials have been investigated, including Niobium, Cuprate, and Magnesium based compositions[40]. YBCO material exhibits strong pinning effects in moderate fields with a critical temperature above that of liquid nitrogen. Thanks to its availability, YBCO bulk superconductors garner academic interest and are actively studied. Other materials have higher critical current densities but also require further cooling due to the lower critical temperatures. YBCO superconductors offer stiff joints for nanosatellites (~1-10 kg) while reducing the cooling power needed to activate flux pinning physics.

The superconductor bulk formation and fabrication impact the stiffness of flux pinning physics within material bounds. Grown from a single crystal, a single domain superconductor yields higher levitation stiffness and exhibits less hysteresis than a granular, epoxy-bonded superconductor. In the context of integrating superconductors on a spacecraft, any cracks or imperfections in the boundary of the superconductor reduce the efficacy of the joint so the superconductor disc should be protected from impact. The superconductor geometry and surface depend on the quality of cut and polish during manufacture. Grain alignment can be adjusted to maximize stiffness in a chosen direction, in which the magnetic moment dipole aligns with the superconductor surface normal.

When sizing the magnet and superconductor, the relative geometry and relative position of the magnet and superconductor determine the strength of the interaction. The flux-pinned interface is optimally stiff when both the diameter of the magnet and the superconductor are similar. Superconductor and magnet size are both bound by manufacturing capabilities, in which superconductor size is more limiting. Although larger superconductor and magnet combinations increase the flux penetrating the superconducting volume, the strength of the interaction does not scale with mass.

The stiffest interaction is achieved through setting an optimal field-cooled orientation, aligning the magnetic moment dipole perpendicular to the superconductor surface, and aligning the grain parallel to the surface. Field-cooled

position depends on lateral and normal separation distance, in which lateral movement is motion parallel to the superconductor plane and normal separation distance is movement perpendicular to the superconductor plane. In designing for field-cooled separation distance, adjusting this separation is a trade between stiffness and collision mitigation. Stiffness in a system with a dipole magnet pinned with the dipole perpendicular to the superconductor surface, when measured along that perpendicular axis is proportional to the field-cooled distance to the 4$^{\text{th}}$ power. The closer distance also reduces the clearance between two spacecraft, which could make collisions more likely. A larger field-cooled distance decreases the stiffness but offers more clearance for a compliant arrest to occur. After the parameters are optimized for performance, the following parameters are studied for model fidelity.

Physical Parameters Affecting Model Fidelity

To inform system level design on dynamics, different physical parameters are studied to evaluate the most dominant characteristics of the flux-pinned system. The dynamics model formulation is explicitly defined, but the physical parameters of the system are rarely exactly known. The important adjustable physical parameters are field-cooled rotation and position, magnet strength, and temperature coefficient, given by Eq. (33). There are some physical characteristics that are inherent to the system and should be optimized outside the context of dynamic modeling, such as the superconductor grain alignment, surface smoothness, and material composition. The state of interest s is the spacecraft's position $[\, x \, y \, z \,]$, velocity $[\, v_x \, v_y \, v_z \,]$, acceleration, quaternion $[\, q_x \, q_y \, q_z \, q_s \,]$, and angular velocity $[\, \omega_x \, \omega_y \, \omega_z \,]$, given by Eq. (34), which are ultimately propagated by force and torque on the system. Dynamic properties of the system include stiffness, natural frequencies and modes, and potential energy.

$$\boldsymbol{p} = \begin{bmatrix} \theta_{FC} \; x_{FC} \; z_{FC} \; B_0 \; c_{temp} \end{bmatrix}^{\text{T}} \tag{33}$$

$$\boldsymbol{s} = \begin{bmatrix} x \; y \; z \; v_x \; v_y \; v_z \; q_x \; q_y \; q_z \; q_s \; \omega_x \; \omega_y \; \omega_z \end{bmatrix}^{\text{T}} \tag{34}$$

The parameters are integrated into the dynamics model by injecting them into frozen image model mapping and state equations. θ_{FC} is the angular displacement from the ideal field-cooled attitude and $[\, x_{FC} \, z_{FC} \,]$ is the position displacement from the ideal field-cooled position, which causes a discrepancy in knowledge of superconductor location and orientation. $[\, \theta_{FC} \, x_{FC} \, z_{FC} \,]$ affect the geometric mapping from source magnet to images, given by Eq. (3) to Eq. (8), and consequently the equilibrium position and orientation of the spacecraft. B_0 is the surface strength of the source magnet, which forms the magnetic moment dipole of the source magnet and the consequential image

mapping. c_t is the scalar coefficient that adjusts the strength of the images depending on the superconductor's temperature, given by Eq. (14) and (15).

These parameters are studied in the context of a single magnet and single superconductor system, then a multiple-magnet and multiple-superconductor system to emphasize the compounding effect and coupled nonlinear dynamics of certain parameters. The parameters operate under different length scales and to avoid unit specific sensitivity analysis, a related numerical parameter is offered with parameters perturbed by one percent.

5. SENSITIVITY STUDY OF DYNAMICS

Single-Magnet and Single-Superconductor System

A common pairing of magnets and superconductors for studying flux pinning dynamics involve Neodymium (NdFeB) permanent magnets and Yttrium Barium Copper Oxide (YBCO) bulk superconductors. All literature referenced in this paper is specific to YBCO material composition, and when relevant, NdFeB magnets. The magnet used in this study is a NdFeB, N42 grade, 0.75 inch diameter spherical magnet of 8815 Gauss manufacturer-specified maximum surface strength. The superconductor disc used in this study is a CAN melt–textured $YBa_2Cu_3O_{7-x}$, single–domain, 56 mm diameter 16 mm thick cylindrical superconductor disc[41]. The magnet is field-cooled at 2.55 cm with its centroid above the center of the superconductor surface and its pole aligned with the superconductor surface normal. The direction convention for studying the single-magnet and single-superconductor (SMSS) system shown in Figure 3.
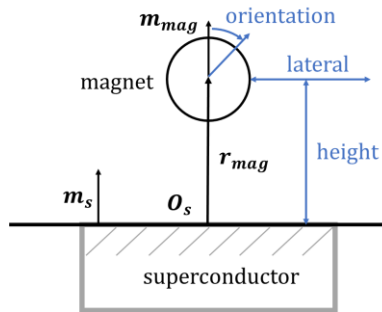
Figure 3: Direction convention for SMSS system.

SMSS Variation of Physical Parameters

To study meaningful variations of physical parameters, relevant parameters are offered to reference for scale. Table 1 summarizes the physical parameters, reference parameters, numerical value of each reference parameter, and numerical value of each physical parameter perturbation. The critical field threshold conditional is assumed to be met and hysteresis is not analyzed. The parameters that encapsulate temperature, geometric and spatial relationship, and physical magnet field strength are all represented explicitly or implicitly in Table 1. The misalignment of the magnet during field-cooling could be up to half the span of full reorientation due to symmetry, from and angle of 0° to 90°. The field-cooled position radial displacement is with respect to the diameter of the superconductor and varies from 0 to 28 mm. The field-cooled position height displacement is with respect to a chosen arbitrary field-cooling height 25.5 mm, from the center of the 19.1 mm diameter magnet to the center of the superconductor, from 9.5 to 41.5 mm. The magnetic field strength of the source magnet is with respect to the manufacturer specified surface field strength, from no strength (0 Gauss) to double the strength (17630 Gauss). Due to dissidence in current literature, temperature variation does not have an accurate model that relates temperature and levitation stiffness. Instead, the temperature variation is captured as a coefficient with respect to 1, from no flux pinning effect (0) to double the effect (2).

Table 1: Summary of Physical Parameters with Relevant Reference Parameters for SMSS system.

Parameter to Vary	Relevant Parameter	Span of Relevant Parameter	Span of Variance
θ_{FC}	Pole to pole orientation	180 deg	[0 to 90] deg
x_{FC}	Diameter of superconductor	56 mm	[0 to 28] mm
z_{FC}	Separation distance/height	25.5 mm	[9.5 41.5] mm
B_0	Magnet surface field strength	8815 G	[0 17630] Gauss
c_t	Temperature coefficient	1	[0 2]

The following section investigates the dynamic response of the system as a result of perturbing these physical parameters. Appropriate metrics to characterize the performance of a flux-pinned interface include stiffness, depth of potential well, natural frequencies, and magnitude of attractive force. The stiffness is the resistance of motion away from equilibrium position or attitude. The potential energy is the energetic capability of the interface to capture a dynamic body and defines the sphere of influence across which the interface acts. Although natural frequency is directly related to stiffness, associating a realistic mass to a stiff joint yields physical intuition to system design.

Magnitude of attractive force is a common metric to compare other physical phenomena acting on spacecraft. The sensitivity is represented as a series of plots across the entire span of each physical parameter with each dynamic response variable normalized to the reference response.

SMSS Sensitivity Results

By linearly varying the physical parameters across the entire span in Table 1, a relationship can be drawn from the magnet's dynamic response and the physical parameters. The following plots are separated by physical parameter. Each plot overlays the lateral stiffness k_l, normal stiffness k_h, rotational stiffness k_θ, potential energy U, and attractive force F normalized to the reference response from the system described in SMSS Physical System. Noise stems from calculations perturbing the magnet state within machine precision error.

When the physical parameter is equivalent to the reference value, the dynamic response is equivalent to the reference response and the normalized reference response is always 1, with reference physical parameters given in Table 2 and reference responses given in Table 3. Table 3 also reports the angular velocity reference response in the lateral ω_l, normal ω_h, and rotational ω_θ directions, which is specific to the mass configuration but physically intuitive. Any normalized values below 1 imply that the reference dynamic model overestimates the actual system's dynamic response, and vice versa for normalized values above 1. Due to the nonlinear behavior of flux-pinned dynamics, some physical parameter variation is amplified despite minimal perturbation. Lateral displacement is the only parameter in which a 1% variation results in less than 1% variation in the consequent dynamic response. When varying the most sensitive physical parameter, field-cooled height, the normal stiffness of the flux-pinned interface changed by over 10%, as shown in Table 4 **Error! Reference source not found.**.

Table 2: Reference Physical Parameters for SMSS system.

Reference Physical Parameter	Physical Parameter Numerical Value
θ_{FC}	0 degrees
x_{FC}	0 m
z_{FC}	0.016 m
B_0	8815 Gauss
c_t	1

Table 3: Reference Dynamic Response Parameters for SMSS system.

Reference Dynamic Response Parameter	Dynamic Response Numerical Value
k_l	29 N/m
k_h	58 N/m
k_θ	0.65 Nm/rad
U	-0.0109 J
F	1.29 N
ω_l	32.7 rad/sec
ω_h	46.5 rad/sec
ω_θ	4.9 rad/sec

The system accumulates error from least sensitive to most sensitive: field-cooled lateral displacement, field-cooled orientation, temperature, magnetic field strength, and field-cooled height. All dynamic response parameters decrease linearly with increasing lateral displacement, with the scalar drawn from experiments measuring magnetic field within a YBCO superconductor disk, as shown in Figure 4 [16]. Note that the reference response already account for the 64% reduction. Varying the field-cooled orientation from perfectly aligned to perfectly misaligned orientation shows monotonic degradation in every dynamic response except for rotational stiffness, which is restored past 45 degrees, as shown in Figure 5. The lateral stiffness was least affected and rotational stiffness was the most affected by orientation perturbation. Normal stiffness, potential energy, and attractive force were similarly degraded by orientation. All dynamic response parameters increase linearly with increasing temperature coefficient, as shown in Figure 6. Temperature and lateral displacement are linear relationships that only affect the images, not the source magnet. All dynamic response parameters increase quadratically with increasing magnetic field strength, not linearly due to magnetic field strength affecting both the source magnet and image strength, as shown in Figure 7. Field-cooled height affects all dynamic response parameters drastically, inversely proportional with z^4, as shown in Figure 8.

Table 4: Percent error in SMSS dynamic response from 1% variation of physical parameters.

		Δx	$\Delta \theta$	Δc	ΔB	Δz
+1% variation in parameter	lateral stiffness k_x % difference	-0.80	-0.01	2.00	4.19	-10.54
	height stiffness k_h % difference	-0.78	0.78	2.33	4.26	-9.69

	rotation stiffness k_θ % difference	-0.80	-1.58	2.00	4.19	-8.53
	potential energy U	-0.80	-0.01	2.00	4.19	-6.46
-1% variation in parameter	lateral stiffness k_x % difference	-0.80	-0.01	-2.00	-3.82	9.24
	height stiffness k_h % difference	-0.78	0.78	-2.33	-3.49	10.08
	rotation stiffness k_θ % difference	-0.80	-1.58	-2.00	-3.82	7.33
	potential energy U	-0.80	-0.01	-2.00	-3.82	5.44
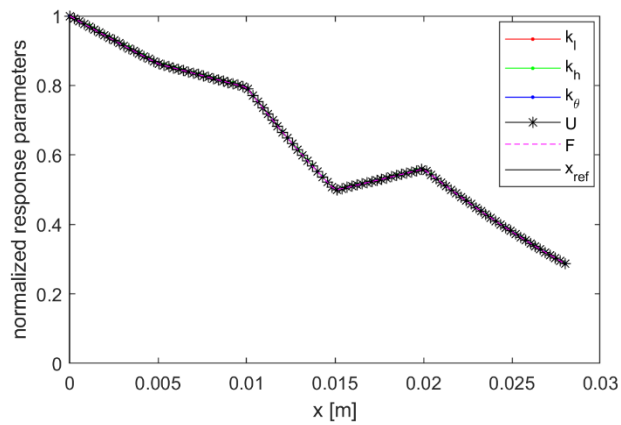
Figure 4: Dynamic response from field-cooled lateral displacement variation.
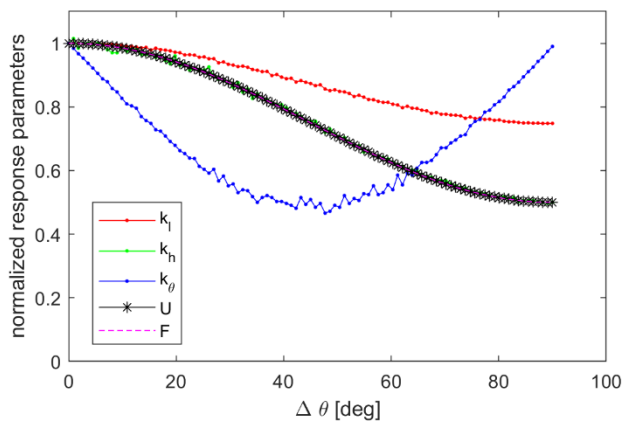
Figure 5: Dynamic response from field-cooled orientation variation.
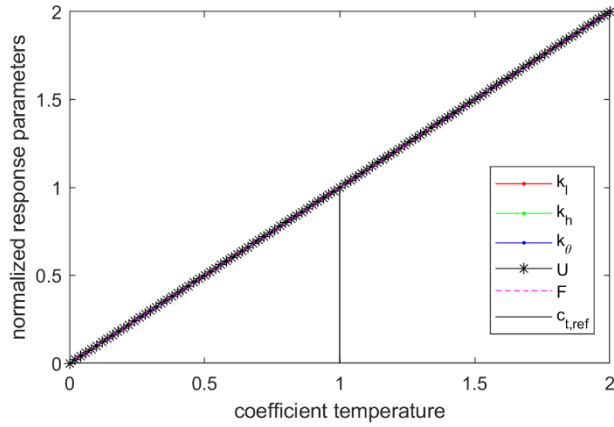
Figure 6: Dynamic response from coefficient of temperature variation.
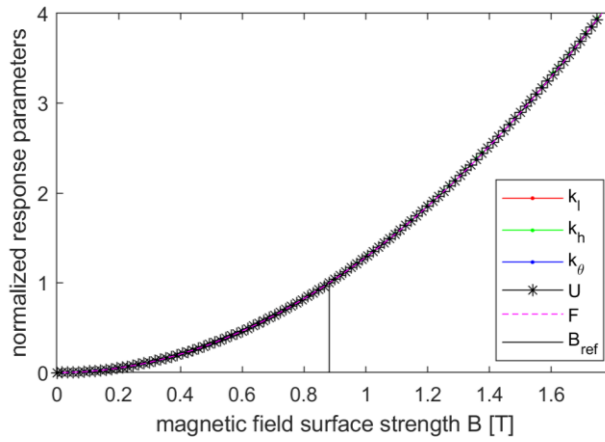
Figure 7: Dynamic response from field-cooled magnetic field strength variation.
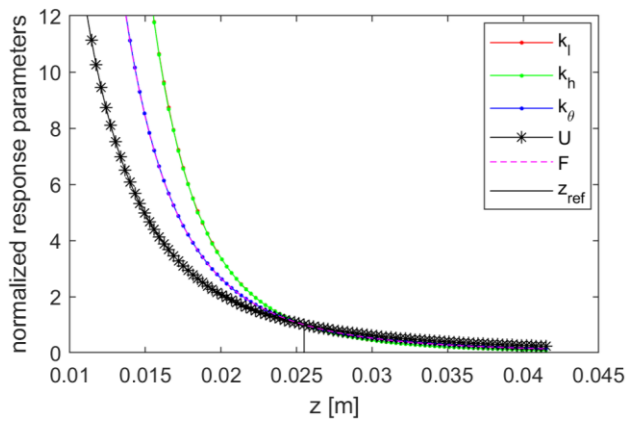
Figure 8: Dynamic response from field-cooled height displacement variation.

Multiple-Magnet and Multiple-Superconductor System

The multiple-magnet and multiple-superconductor (MMMS) interface uses the same components and physical parameters described in the SMSS Physical System section but involves three superconductors and twelve magnets. In a case studying two spacecraft for a docking application, we define the magnetic spacecraft with a mass of 2.1 kg, 20.3 cm diameter sphere with full range of motion and the superconducting spacecraft of significantly more volume and mass with no motion. The magnets are arranged in an icosahedron geometry, in which all magnets are pointing radially outward and equidistant from each neighboring magnet. This symmetric magnetic configuration allows the spherical spacecraft to be captured in any arbitrary attitude. The superconductors are placed so that any trio of the magnetic spacecraft's magnets are 2.55 cm radially inward in equilibrium position and pointed along the radial direction. This interface has been tested on a series of testbeds to study docking and capture dynamics, as shown in Figure 9[1]. Using the same dynamic response parameters, lateral, normal, and rotational directions must be defined similarly to the single magnet and single superconductor system, also shown in Figure 10.
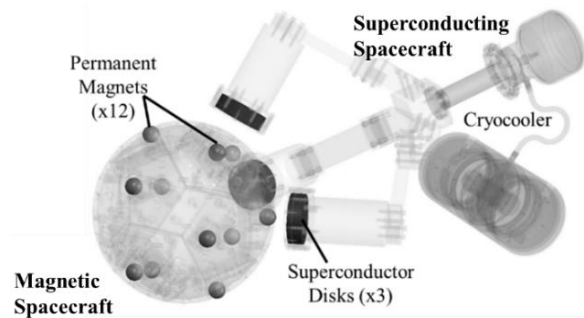

Figure 9: Multiple magnet and multiple superconductor flux-pinned interface of docking interface concept.
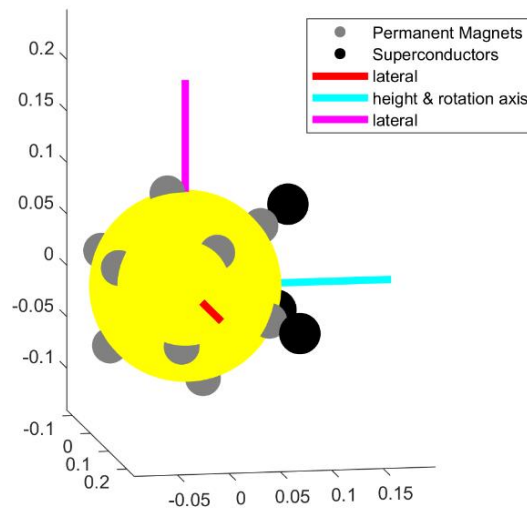

Figure 10: Direction convention for MMMS system.

MMMS Variation of Physical Parameters

Although the physical parameter symbols are analogous to the SMSS system, $\theta_{FC}, x_{FC}, z_{FC}$ represent slightly different physical parameters relating to the spacecraft, not an individual magnet. θ_{FC} is the angular displacement between two equilibria rotated about the center of the superconductors. As the spacecraft rotates about this axis, the magnets move off the superconductor surface at 16.5 deg. The lateral separation distance, x_{FC}, between the magnetic spacecraft and the superconducting spacecraft spans from equilibrium position to physical interference between the two spacecraft bodies, symmetric in either direction. The lateral displacement never allows the magnet to move off the surface area of the superconductor because the two spacecraft surfaces interfere before the magnet moves too far in the lateral direction. The normal separation distance, magnetic field strength, and temperature coefficient cover the same spans. Table 5 lists all parameters and the corresponding span of variance.

Table 5: Summary of Physical Parameters with Relevant Reference Parameters for MMMS system.

Parameter to Vary	Relevant Parameter	Numerical Value of Relevant Parameter	Span of Variance
θ_{FC}	Angular displacement between spacecraft EQ orientation	16.5 deg	[0 16.5] deg
x_{FC}	Lateral separation distance	8.5 mm	[0 8.5] mm
z_{FC}	Normal separation distance	25.5 mm	[-16 16] mm
B_0	Magnet surface field strength	8815 G	[0 17630] Gauss
c_t	Temperature coefficient	1	[0 2]

MMMS Sensitivity Results

By linearly varying the physical parameters across the entire span in Table 5, a relationship can be drawn from the spacecraft's dynamic response and the physical parameters. The reference physical parameters are given in Table 6 and the reference responses are given in Table 7. Like the SMSS system, the parameters listed in Table 5 represent all proposed modifications in modeling the flux pinning interaction, outside of hysteresis and material properties. Unlike the SMSS system, the MMMS rotational and translational degrees of freedom are coupled due to the source magnet and superconductor orientations spanning $\mathbb{R}^3$. The MMMS system is stiffer than the SMSS system in the translational degrees of freedom, but less stiff in rotation. The baseline rotational stiffness is very low and any modifications to the system, like translational perturbation, transfers stiffness in translation to stiffness in rotation. Any perturbation in the system is amplified in the dynamic response to different degrees, as shown in Table 8. The

most sensitive dynamic response is rotational stiffness. The physical parameter causing the most drastic change in a single dynamic response parameter is field-cooled orientation, but the change in the other dynamic responses are minimal. The physical parameter that affected the most distributed change across the entire system is field-cooled height.

The system manifests the most error in any single dynamic response from least sensitive to most sensitive: temperature, magnetic field strength, field-cooled height, field-cooled lateral displacement, and field-cooled orientation, as shown in Table 8. The system accumulates the most error across all dynamic responses, from least sensitive to most sensitive, in temperature, field-cooled lateral displacement, magnetic field strength, field-cooled height, and field-cooled orientation, as shown in Table 9**Error! Reference source not found.**. Temperature and magnetic field vary the MMMS system in the same way that they did in the SMSS system because these parameters are agnostic to specific geometries. Temperature and magnetic field affect all magnet-superconductor interactions equally, seen in Figure 11 and Figure 12. The other physical parameters require a specific geometry context to explain the change in dynamic response.

Table 6: Reference Physical Parameters for MMMS system.

Reference Physical Parameter	Physical Parameter Numerical Value
θ_{FC}	0 degrees
x_{FC}	0 m
z_{FC}	0.016 m
B_0	8815 Gauss
c_{temp}	1

Table 7: Reference Dynamic Response Parameters for MMMS system.

Reference Dynamic Response Parameter	Dynamic Response Numerical Value
k_l	65 N/m
k_h	89 N/m
k_θ	0.304 Nm/rad

U	0.0497 J
F	1.8137 N
ω_l	5.57 rad/sec
ω_h	6.53 rad/sec
ω_θ	0.38 rad/sec

The geometry specific parameters include field-cooled lateral displacement, height, and orientation. The lateral displacement, symmetric in the negative and positive directions, shifts one magnet-superconductor closer together in the surface normal direction. The opposite is true for the other magnet-superconductor pairs, which slides each magnet laterally across the corresponding superconductor surfaces. Although two of the three magnet-superconductor pair interactions are weaker, the closer magnet-superconductor more than compensates for the other reductions by increasing strength with z^3, increasing normal and lateral stiffness, seen in Figure 13. Rotational stiffness depends on the lateral stiffness of individual magnet-superconductor pairs and scales with less than a z^3 interaction. The field-cooled height for the spacecraft shifts every magnet superconductor pair equally, in a combination of normal and lateral direction with respect to each superconductor surface. The spacecraft dynamic responses are predictably stronger as the magnetic spacecraft is field-cooled closer to the superconducting spacecraft, seen in Figure 14. The MMMS system does not behave as dramatically to height variation as the SMSS system because the individual magnets also move in the lateral direction along the superconductor surface, reducing the amount of flux penetrating each superconductor. At the reference field-cooled orientation, the magnet-superconductor pairs are aligned, but as the field-cooled orientation is perturbed, the magnet-superconductor pairs are misaligned, causing a reduction in lateral and height stiffness. The magnetic moment dipoles begin to align with the superconductor surface tangent, contributing to an increase in rotational stiffness. With further angular displacement, the magnet is farther from the superconductor center in both lateral and normal distance, seen in Figure 15.

Table 8: Percent error in MMMS dynamic response from 1% variation in each physical parameter.

|		Δx	$\Delta\theta$	Δc	ΔB	Δz
+1% variation in parameter	lateral stiffness k_x % difference	1.67	4.63	3.90	-1.46	-4.66
	height stiffness k_h % difference	2.87	6.09	7.06	4.14	-1.85

	rotation stiffness k_θ % difference	2.51	15.91	22.75	24.39	45.66
	potential energy U	2.00	2.00	2.63	-0.22	-0.47
	attractive force F	2.00	4.59	2.58	-0.22	-0.47
-1% variation in parameter	lateral stiffness k_x % difference	-2.37	-3.33	-4.72	-1.46	-4.66
	height stiffness k_h % difference	-1.21	-2.21	-5.35	4.14	-1.85
	rotation stiffness k_θ % difference	-0.75	-3.33	10.76	24.39	45.66
	potential energy U	-3.42	-2.00	-4.28	-0.22	-0.47
	attractive force F	-3.42	-2.00	-4.34	-0.22	-0.47

Table 9: Accumulated percent error in dynamic response from 1% variation in each physical parameter.

|	Δx	$\Delta \theta$	Δc	ΔB	Δz
Accumulated percent error over all dynamic responses due to +1% variation in parameter	11.05	30.42	33.23	38.92	53.10
Accumulated percent error over all dynamic responses due to -1% variation in parameter	11.17	30.42	12.87	29.44	53.10
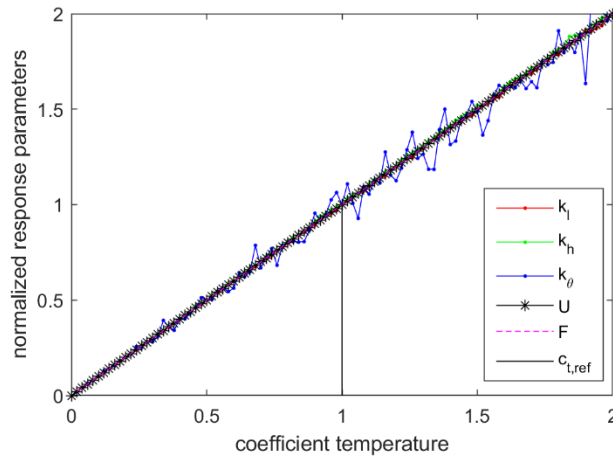
Figure 11: Dynamic response of system due to temperature coefficient variation.
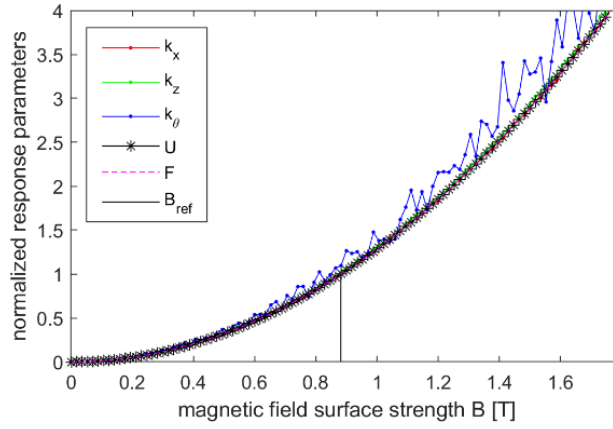
Figure 12: Dynamic response of system due to magnetic field strength variation.
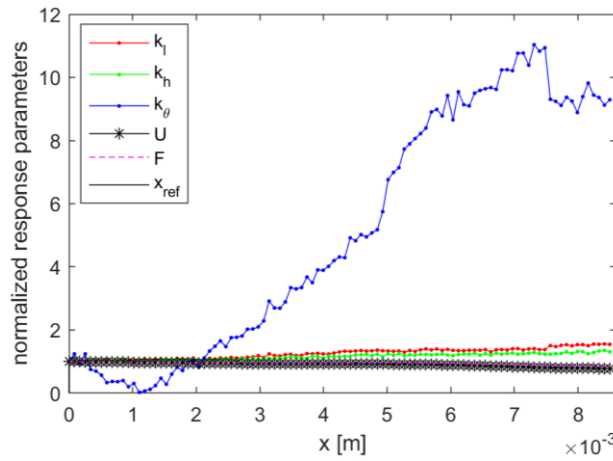
Figure 13: Dynamic response of system due to lateral displacement variation.
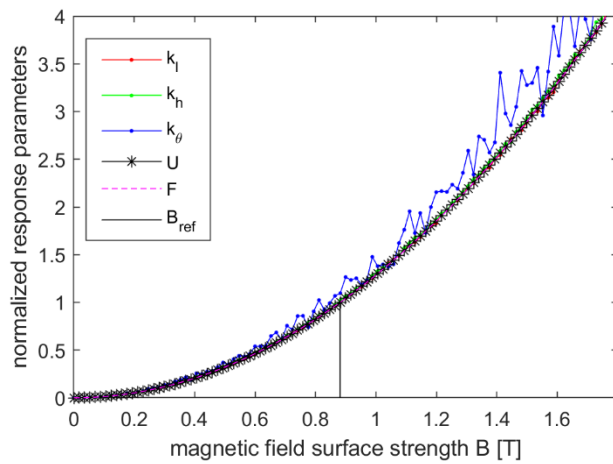
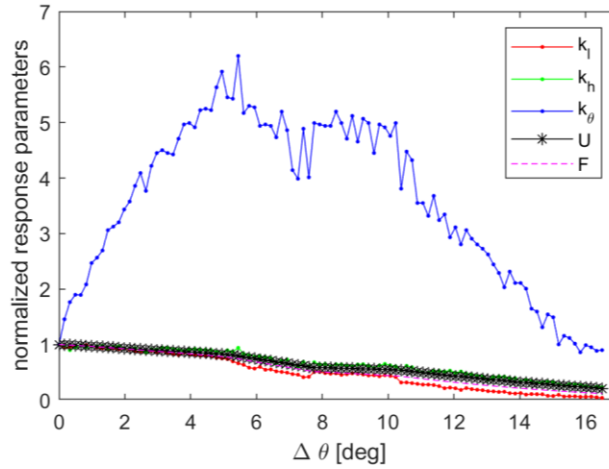**Figure 14: Dynamic response of system due to height variation.**

Figure 15: Dynamic response of system due to field-cooled angle displacement variation.

6. CONCLUSIONS

In this paper, many modifications are suggested to refine Kordyuk's frozen image model, which is a less computationally intensive alternative to the critical state model. These modifications are based upon empirical data that explain discrepancies between an ideal and physical system. The refinements are expressed in analytical form and injected into a dynamics model simulating flux-pinned interface dynamics. Although the refinements add more computation, the order of computation of the refined model is on the order of $\sigma(16MN^2)$ vs. the baseline order of $\sigma(2MN^2)$, which is still significantly less intensive than the critical state model. Two systems, based on commercially available components, are described to form a baseline dynamic response for a single-magnet single-superconductor system and multiple-magnet multiple-superconductor system. A sensitivity study is performed on each system to probe the effect of different physical parameters on the dynamic response of the system.

From the sensitivity study, system-level design considerations may be formed to target less error or emphasize certain dynamic responses. Some parameters are not geometry specific, like temperature and magnetic field strength, but all field-cooled parameters are geometry specific. In general, the field-cooled separation distance affects the system performance most significantly. When designing, integrating, or validating the specifications of a physical system, trade-offs are made weighing different dynamic characteristics, which are adjusted with knowledge of the consequences from each physical parameter. For example, interface stiffness is the resistance of the two bodies to separate for which higher stiffness implies a more robust joint. An implication of stiffness is also natural resonant frequency for which either the interface can excite unwanted vibration in the individual spacecraft or spacecraft

components can excite the interface unstably. Realistically at the mass of small satellites and the strongest permanent magnets, the natural frequencies range from 10's of Hz to single Hz in magnitude, which must be considered for low and high frequency jitter. Outside control of system design, this sensitivity study informs technologists observing flux-pinning dynamics of potential sources and magnitudes of error from each physical parameter. In developing flux-pinned technology, this paper demonstrates the need to measure or control certain parameters with more precision to guarantee predictable dynamics below certain error bounds.

ACKNOWLEDGEMENTS

REFERENCES

1 Zhu, F., Jones-Wilson, L., and Peck, M., "Capturing and Docking Spacecraft with Flux Pinned Interfaces," Guadalajara, Mexico: 2016.
2 Jones, L., and Peck, M., "Stability and Control of a Flux-Pinned Docking Interface for Spacecraft," *AIAA Guidance, Navigation, and Control Conference*, American Institute of Aeronautics and Astronautics.
3 Shoer, J. P., and Peck, M. A., "Flux-Pinned Interfaces for the Assembly, Manipulation, and Reconfiguration of Modular Space Systems," *The Journal of the Astronautical Sciences*, vol. 57, Jul. 2009, pp. 667–688.
4 Shoer, J., and Peck, M., "Simulation of Multibody Spacecraft Reconfiguration through Sequential Dynamic Equilibria," *AIAA Guidance, Navigation, and Control Conference*, American Institute of Aeronautics and Astronautics.
5 Gersh, J., "Architecting the Very-Large-Aperture Flux-Pinned Space Telescope: A Scalable, Modular Optical Array with High Agility and Passively Stable Orbital Dynamics," *AIAA/AAS Astrodynamics Specialist Conference and Exhibit*, American Institute of Aeronautics and Astronautics.
6 Jones, L., "Prospects and Challenges of Particulate Solar Sail Propulsion," *AIAA/AAS Astrodynamics Specialist Conference and Exhibit*, American Institute of Aeronautics and Astronautics.
7 Norman, M. C., and Peck, M. A., "Simplified Model of a Flux-Pinned Spacecraft Formation," *Journal of Guidance, Control, and Dynamics*, vol. 33, 2010, pp. 814–822.
8 Wilson, W., Shoer, J., and Peck, M., "Demonstration of a Magnetic Locking Flux-Pinned Revolute Joint for Use on CubeSat-Standard Spacecraft," *AIAA Guidance, Navigation, and Control Conference*, American Institute of Aeronautics and Astronautics.
9 Shoer, J., and Peck, M., "Reconfigurable Spacecraft as Kinematic Mechanisms Based on Flux-Pinning Interactions | Journal of Spacecraft and Rockets," *Journal of Spacecraft and Rockets*, vol. 46, 2009, pp. 466–469.
10 Shoer, J., Wilson, W., Jones, L., Knobel, M., and Peck, M., "Microgravity Demonstrations of Flux Pinning for Station-Keeping and Reconfiguration of CubeSat-Sized Spacecraft | Journal of Spacecraft and Rockets," *Journal of Spacecraft and Rockets*, vol. 47, 2010, pp. 1066–1069.
11 Norman, M. C., and Peck, M. A., "Stationkeeping of a Flux-Pinned Satellite Network," *Journal of Guidance, Control, and Dynamics*, vol. 33, 2010, pp. 1683–1687.
12 Sanchez, A., and Navau, C., "Vertical force, magnetic stiffness and damping for levitating type-II superconductors," *Physica C: Superconductivity*, vol. 268, Sep. 1996, pp. 46–52.
13 Kordyuk, A. A., "Magnetic levitation for hard superconductors," *Journal of Applied Physics*, vol. 83, Jan. 1998,

pp. 610–612.

[14] Sanchez, A., and Navau, C., "Critical-current density from magnetization loops of finite high- T c superconductors," *Superconductor Science and Technology*, vol. 14, 2001, p. 444.

[15] Teshima, H., Sawamura, M., Morita, M., and Tsuchimoto, M., "Levitation forces of a single-grained Y-Ba-Cu-O bulk superconductor of 48 mm in diameter," *Cryogenics*, vol. 37, 1997, pp. 505–509.

[16] Zhu, F., Peck, M., and Jones-Wilson, L., "Reduced Embedded Magnetic Field in Type II Superconductor of Finite Dimension," *in submission to IEEE Transactions on Applied Superconductivity*.

[17] Navau, C., Sanchez, A., Pardo, E., and Chen, D.-X., "Equilibrium positions due to different cooling processes in superconducting levitation systems," *Superconductor Science and Technology*, vol. 17, 2004, p. 828.

[18] Zhang, X.-Y., Zhou, Y.-H., and Zhou, J., "Modeling of symmetrical levitation force under different field cooling processes," *Physica C: Superconductivity*, vol. 468, Mar. 2008, pp. 401–404.

[19] Yang, Y., and Zheng, X., "Method for solution of the interaction between superconductor and permanent magnet," *Journal of Applied Physics*, vol. 101, Jun. 2007, p. 113922.

[20] Brandt, E. H., "Friction in levitated superconductors," *Applied Physics Letters*, vol. 53, Oct. 1988, pp. 1554–1556.

[21] Brandt, E. H., "Rigid levitation and suspension of high-temperature superconductors by magnets," *American Journal of Physics*, vol. 58, Jan. 1990, pp. 43–49.

[22] Zhang, X.-Y., Zhou, Y.-H., and Zhou, J., "Effects of magnetic history on the levitation characteristics in a superconducting levitation system," *Physica C: Superconductivity and its Applications*, vol. 468, Jul. 2008, pp. 1013–1016.

[23] Yang, W. M., Zhou, L., Feng, Y., Zhang, P. X., Zhang, C. P., Yu, Z. M., Tang, X. D., Nicolsky, R., and Andrade, R., "Identification of the effect of grain size on levitation force of well-textured YBCO bulk superconductors," *Cryogenics*, vol. 42, Oct. 2002, pp. 589–592.

[24] Yang, W. M., Zhou, L., Feng, Y., Zhang, P. X., Zhang, C. P., Yu, Z. M., and Tang, X. D., "Effect of perimeters of induced shielding current loops on levitation force in melt grown single-domain YBa2Cu3O7−x bulk," *Applied Physics Letters*, vol. 79, Sep. 2001, pp. 2043–2045.

[25] Landecker, P. B., Villani, D. D., and Yung, K. W., "An Analytic Solution for the Torque Between Two Magnetic Dipoles," *Physical Separation in Science and Engineering*, 1999.

[26] Yung, K. W., Landecker, P. B., and Villani, D. D., "An Analytic Solution for the Force Between Two Magnetic Dipoles," *Physical Separation in Science and Engineering*, 1998.

[27] Zhu, F., and Peck, M., "Linearized Dynamics of General Flux-Pinned Interfaces," *IEEE Transactions on Applied Superconductivity*, vol. 28, Dec. 2018, pp. 1–10.

[28] Chiang, C. H., Yang, C. W., Hsieh, P. L., and Chan, W. C., "Levitation Force Measurement at Different Temperatures for YBCO Superconductor," *Journal of Low Temperature Physics*, vol. 131, May 2003, pp. 743–746.

[29] Jiang, H., Wang, J., Wang, S., Ren, Z., Zhu, M., Wang, X., and Shen, X., "The magnetic levitation performance of YBaCuO bulk at different temperature," *Physica C: Superconductivity*, vol. 378–381, Oct. 2002, pp. 869–872.

[30] Halbritter, J., "Granular superconductors and their intrinsic and extrinsic surface impedance," *Journal of Superconductivity*, vol. 8, Dec. 1995, pp. 691–703.

[31] Jones, L., "The Dynamics and Control Of Flux-Pinned Space Systems: Theory And Experiment," Cornell, 2012.

[32] Liang, R., Dosanjh, P., Bonn, D. A., Hardy, W. N., and Berlinsky, A. J., "Lower critical fields in an ellipsoid-shaped YBCO single crystal," *Physical Review B*, vol. 50, Aug. 1994, pp. 4212–4215.

[33] Chan, W. C., Wang, C. Y., and Lee, J. J., "Grain size effect on magnetic levitation of YBCO superconducting samples," *Physica C: Superconductivity*, vol. 282–287, Aug. 1997, pp. 1455–1456.

[34] Yang, W. M., Zhou, L., Feng, Y., Zhang, P. X., Chen, S., Wu, M. Z., Zhang, C. P., Wang, J. R., Du, Z. H., Wang, F. Y., Yu, Z. M., Wu, X. Z., Gawalek, W., and Gornert, P., "The grain-alignment and its effect on the levitation force of melt processed YBCO single-domained bulk superconductors," *Physica C: Superconductivity*, vol. 307, Oct. 1998, pp. 271–276.

[35] Yang, W. M., Feng, Y., Zhou, L., Zhang, P. X., Wu, M. Z., Chen, S., Wu, X. Z., and Gawalek, W., "The effect of the grain alignment on the levitation force in single domain YBa2Cu3Oy bulk superconductors," *Physica C: Superconductivity*, vol. 319, Jun. 1999, pp. 164–168.

[36] Yang, W. M., Zhou, L., Feng, Y., Zhang, P. X., Zhang, C. P., Nicolsky, R., and Jr, R. de A., "The effect of different field cooling processes on the levitation force and attractive force of single-domain YBa 2 Cu 3 O 7− x bulk," *Superconductor Science and Technology*, vol. 15, 2002, p. 1410.

[37] Alqadi, M. K., Alzoubi, F. Y., Al-khateeb, H. M., and Ayoub, N. Y., "Interaction between a point magnetic dipole and a high-temperature superconducting sphere," *Physica B: Condensed Matter*, vol. 404, Jun. 2009, pp. 1781–1784.

[38] Ren, Z., Wang, J., Wang, S., Jiang, H., Zhu, M., Wang, X., and Song, H., "Influence of shape and thickness on the levitation force of YBaCuO bulk HTS over a NdFeB guideway," *Physica C: Superconductivity*, vol. 384, Jan. 2003, pp. 159–162.

[39] Yang, W. M., Zhou, L., Feng, Y., Zhang, P. X., Wang, J. R., Zhang, C. P., Yu, Z. M., Tang, X. D., and Wei, W., "The effect of magnet configurations on the levitation force of melt processed YBCO bulk superconductors," *Physica C: Superconductivity*, vol. 354, May 2001, pp. 5–12.

[40] Chaddah, P., "Critical current densities in superconducting materials," *Sadhana*, vol. 28, Feb. 2003, pp. 273–282.

[41] "Levitation bulk," *CAN SUPERCONDUCTORS* Available: http://www.can-superconductors.com/levitation-bulk.html.

Biography

Frances Zhu earned her B.S. in Mechanical and Aerospace Engineering in 2014 and her Ph.D. in Aerospace Engineering in 2019, all at Cornell University, Ithaca. Since 2014, she has been a Research Assistant with the Space Systems Design Studio, specializing in dynamics, systems, and controls engineering. Her research interests include flux pinned interface applications, spacecraft system architectures, robot dynamics, estimation, and controls. Ms. Zhu is a NASA Space Technology Research Fellow.

Mason A. Peck earned a B.S. in Aerospace Engineering from the University of Texas at Austin. He worked at Bell Helicopter from 1993 to 1994 on structural dynamics. From 1994 to 2001 he was an attitude dynamics specialist and systems engineer at Hughes Space and Communications (now Boeing Satellite Systems). During his years at Boeing he served as attitude dynamics lead in the Boeing mission control center, participating in real-time spacecraft operations and helping to resolve spacecraft performance anomalies. He earned his M.S. and Ph.D. at UCLA as a Howard Hughes Fellow from 1998 to 2001. In 2001 he joined Honeywell Defense and Space Systems, and in 2003 was named Principal Fellow. He has been issued several patents. In July of 2004, he joined the faculty at Cornell University, where he teaches courses in dynamics and control and in the mechanical and aerospace engineering program. He was promoted to Associate Professor in fall 2010. In 2012, he was appointed as NASA's Chief Technologist.

Laura Jones-Wilson earned her Bachelor of Science in aerospace engineering with a minor in mathematics in 2007. Laura graduated in the summer of 2012 with her Ph.D. in Aerospace Engineering, with a concentration in Dynamics and Controls and a minor in Astronomy. She was awarded both the National Science Foundation (NSF) Graduate and the National Defense Science and Engineering Graduate (NDSEG) Fellowship. Presently, Dr. Jones-Wilson is a Guidance and Control Systems Engineer at NASA Jet Propulsion Laboratory.